Received: 27 March 2022 | Revised: 30 August 2022 | Accepted: 1 September 2022

DOI: 10.1002/htj.22741

ORIGINAL ARTICLE

HEAT TRANSFER WILEY

Effect of triangular porous layer on the transfer of heat and species in a channel-open cavity

Ali Q. Abd Al-Hassan | **Muneer A. Ismael**

Mechanical Engineering Department, College of Engineering, University of Basrah, Basrah, Iraq

Correspondence
Muneer A. Ismael, Mechanical Engineering Department, College of Engineering, University of Basrah, Basrah 61004, Iraq.
Email: muneer.ismael@uobasrah.edu.iq

Abstract

This paper addresses the heat and species transfer in a composite cavity linked with a horizontal channel. The cavity comprises a triangular porous layer and one of its vertical sides is exposed to a high temperature and concentration. The mathematical conservation equations are solved numerically using the Galerkin finite element method. The ranges of Reynolds and Richardson numbers are taken to ascertain laminar flow, $Re = 50–250$ and $Ri = 0.1–100$. The size of the porous layer is quantified by the thickness of the porous layer $H_p = 0.25–1$. The problem is studied for two cases of heat and species sources; the opposing case, when the active side is on the right, and assisting case, when the active side is on the left. Results reveal that for specified conditions, the triangular porous layer increases Nusselt and Sherwood numbers by 30% and 32%, respectively, more than the horizontal porous layer. The opposing case gives maximum convective heat transfer, where for $Ri = 0.01$, the Nusselt number is higher by 61% and 134% for $Re = 50$ and 250, respectively, while for $Ri = 100$, the percentages increase are 67% and 43%.

KEYWORDS

Brinkman model, channel, double diffusive, inclined interface, open cavity, triangular porous layer

1 | INTRODUCTION

Transfer of heat and species in a partially porous cavity linked to a rectangular channel is observed in diverse applications such as the absorber of the solar turbine, filtration, cooling of electronic devices, photovoltaic sheets, and geophysical problems.[1] In a solar turbine, a chimney is connected at the center of a large circular solar collector. A porous layer is inserted as a base of the solar collector to receive more radiation and this leads to sucking more air from the circumference of the collector to pass through the chimney and drive the turbine. An example of the most interesting studies of such a problem is the simulation work of Manca et al.[2] who inspected three different cases of heating an open cavity filled with clear fluid. The cases were distinguished by which wall of the cavity is set as the source of heat. The results showed that the maximum temperature values decreased as Reynolds and Richardson's numbers increased. In addition, they showed that the Nusselt number and the maximum temperature satisfied the performance demand when the source of heat is set at the vertical wall of the cavity, which is opposite to the direction of flow in the channel. Leong et al.[3] studied the convection in an open cavity heated from the base and exposed to an external flow. They observed that when the forced flow is dominant, the rate of heat exchange declines while the flow becomes unstable. Brown and Lai[4] investigated the correlations for convective heat and mass transfer from an open cavity including the related Prandtl number with the heat and mass transfer. They predicted that the correlations for other working fluids would have similar figures but with other coefficients that can be predicted by computations or experiments in the future. Manca et al.[5] prepared experimental studies of mixed convection inside an open cavity with a heated wall bounded by a horizontal unheated sheet. The heated sheet faces (opposite) the direction of flow in the channel. For low Re numbers, they observed flow penetration into the cavity. Aminossadati and Ghasemi[6] conducted a study dealing with convective heat exchange in a channel linked with an open cavity. A heat source segment was assumed in three individual positions (bottom, right, and left) of the cavity. The right position which faces the channel-flow direction displayed the best heat transfer. Buonomo et al.[7] considered the nonlocal thermal equilibrium in a cavity filled with a metal foam and linked with a horizontal channel. It seems that Buonomo et al.[7] have endorsed the findings of previous research, where they set the heat source on one of the vertical walls of the cavity. The results displayed that the temperature of the fluid phase is higher than that of the solid phase and they attributed this result based on the diffusive effect in both phases. Nasrin et al.[8] considered the nonuniform heating from the base of a porous cavity saturated with titanium oxide–water nanofluid and linked to a horizontal channel. Buonomo et al.[9] studied experimentally the convective heat exchange of a channel involving a foam layer set at the lower wall of the channel. They showed that higher porosity foam could lower the average temperature of the heated wall, hence they deduced a beneficial role of the presence of the foam layer mainly at a high Reynolds number. Carozza et al.[10] simulated the convective heat transfer in a cavity linked with a channel. The cavity had two vertical walls at uniform temperatures. They observed the familiar increase of the average Nusselt number and decrease of the average temperature with the Reynolds number. Also, their results confirmed the proportionality relation between Reynolds and Nusselt numbers, which is stronger for the opposing case. Sabbar et al.[11] suggested a different strategy for the cavity linked with a channel where the active opposing wall is made of flexible material. This strategy gave rise to the Nusselt number better than the conventional rigid wall.

Vented porous cavities manifest identical mixed-mode heat transfer as in the cavity linked with a channel. Therefore, it is worth mentioning the most important studies regarding this

topic. Saeid[12] analyzed the influence of convective heat transfer effect by a porous layer inserted inside a vented enclosure, by assuming nonlocal thermal equilibrium between the fluid and the solid matrix of the porous layer. Shi and Vafai[13] performed a numerical of convective heat transfer inside a porous cavity involving an obstruction. The cavity was heated from the base. Maougal and Bessaih[14] focused on the influence of convective heat transfer intensity, and porous media on the transfer of heat and the generated thermodynamic irreversibility. Mojumder et al.[15] investigated the convective heat transfer in a lid-driven porous cavity formed in L-shaped geometry. Gibanov et al.[16] considered the mixed convection inside a vented cavity involving a triangular porous layer with discreet heating from below.

Recently, Abd Al-Hassan and Ismael[17] focused on the transfer of mass and heat in a composite open cavity linked with a horizontal channel. A porous layer with a specified thickness is inserted in the cavity and two cases of considering the active cavity walls were investigated. They also endorsed the benefit of opposing active walls over the assisting ones. More recently, the works of Almuhtady et al.[18] and Abderrahmane et al.[19] have revealed the importance of mixed convection in complex enclosures driven by moving walls and rotating cylinders, respectively.

Regarding the forced cooling by a fluid stream, previous works have only focused on plane porous layers. Thus, the present work investigates how the inclined porous layer affects the transfer of heat and mass (drying) when subjected to a cold and dry stream. Such a problem is a simulation for the porous absorber of a solar collector used in a solar turbine. Despite the interest in such a problem, no one, as far as we know, has studied it. Indeed, this problem is a continuing study of our previous paper[17] regarding a horizontal porous layer. In this study, we investigate the effect of a triangular porous layer inserted in a cavity linked with a channel. The opposing and assisting cases are also inspected with this inclined layer.

2 | PROBLEM MODELING

A schematic illustration of the current problem is portrayed in Figure 1. It comprises an open cavity linked with a horizontal channel. A triangular porous layer occupies a part of the cavity where the vertical side coincides with the left wall of the cavity while the base coincides with the base of the cavity. The length of the vertical side of the triangular porous layer, H_p, is varied to quantify the effect of the porous layer size. High temperature, T_H, and high species, c_H are set on either the cavity vertical left side (assisting case) or the right side (opposing case). Adiabatic conditions were set on the remainder solid walls. Fluid flows through the channel where it enters with a uniform velocity u_{in}, low temperature, T_C, and low concentration, c_L. Assuming the flowing fluid is water at an average temperature of 22°C, we set the Prandtl number at 6.24 and ignored the compressibility of water. By taking the height of the channel H as a characteristic length, the geometrical dimensions are based on Figure 1. The normal dimension is taken very long, thus the problem is minimized to two-dimensional. The parameters of Reynolds and Rayleigh numbers were limited within the laminar regime. The dissipation of energy and radiation between surfaces is omitted. The model of Darcy–Brinkman (in which the dynamic viscosities of fluids inside and out of the porous layer are taken equal[20]) is used for the porous domain. The solid matrix is assumed to form a porosity of $\varepsilon = 0.398$ and thermal conductivity of $k_p = 0.845\,\mathrm{W/m\,K}$.[21] Therefore, the effective thermal conductivity of the porous medium is calculated from the mixing relation, $k_{eff} = k_p(1-\varepsilon) + \varepsilon k_f = 0.7507\,\mathrm{W/m\,K}$ where

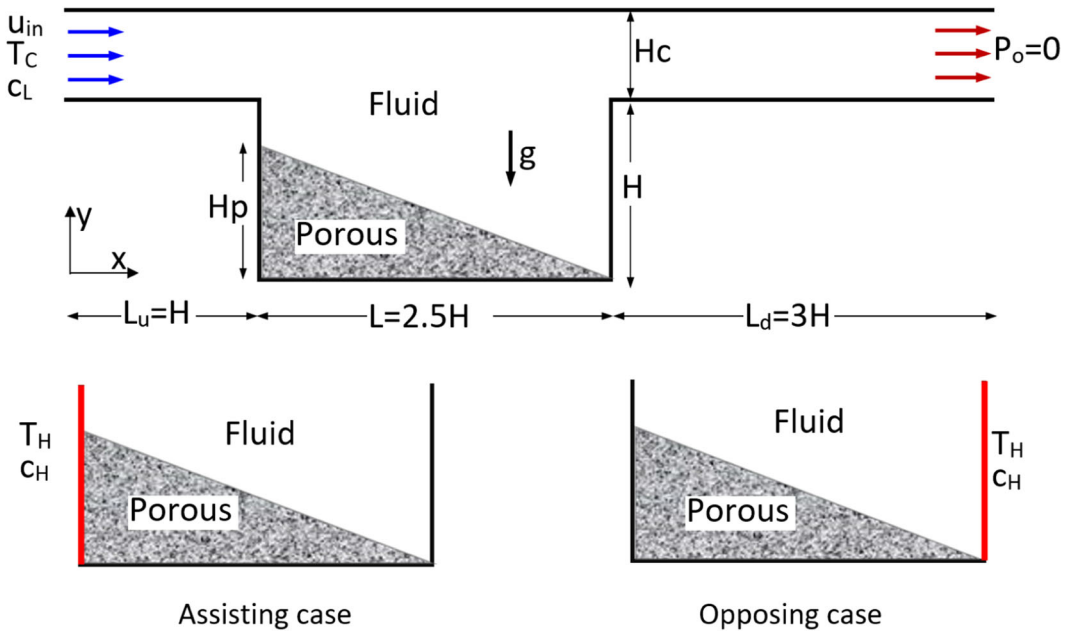

FIGURE 1 Schematic diagram and coordinates arrangements of the present problem. [Color figure can be viewed at wileyonlinelibrary.com]

the thermal conductivity of water at 22°C is 0.608 W/m K. Based on the conclusions of Manca and colleagues,[2,6,10] heating from the cavity base is not considered in this study.

The governing equations in the dimensionless form are written for both media, porous and clear fluid, are cast as:[21]

2.1 | Clear fluid

Continuity:

$$\frac{\partial U_f}{\partial X} + \frac{\partial V_f}{\partial Y} = 0. \tag{1}$$

X-direction momentum equation:

$$\frac{\partial U_f}{\partial \tau} + \left(U_f \frac{\partial U_f}{\partial X} + V_f \frac{\partial U_f}{\partial Y}\right) = -\frac{\partial P}{\partial X} + \frac{1}{Re}\left(\frac{\partial^2 U_f}{\partial X^2} + \frac{\partial^2 U_f}{\partial Y^2}\right). \tag{2}$$

Y-direction momentum equation:

$$\frac{\partial V_f}{\partial \tau} + \left(U_f \frac{\partial V_f}{\partial X} + V_f \frac{\partial V_f}{\partial Y}\right) = -\frac{\partial P}{\partial Y} + \frac{1}{Re}\left(\frac{\partial^2 V_f}{\partial X^2} + \frac{\partial^2 V_f}{\partial Y^2}\right) + Ri\theta + NRiC. \tag{3}$$

Energy equation:

$$\frac{\partial \theta_f}{\partial \tau} + U_f \frac{\partial \theta_f}{\partial X} + V_f \frac{\partial \theta_f}{\partial Y} = \frac{1}{RePr}\left(\frac{\partial^2 \theta_f}{\partial X^2} + \frac{\partial^2 \theta_f}{\partial Y^2}\right). \tag{4}$$

Mass equation of species:

$$\frac{\partial C_f}{\partial \tau} + U_f \frac{\partial C_f}{\partial X} + V_f \frac{\partial C_f}{\partial Y} = \frac{1}{RePrLe}\left(\frac{\partial^2 C_f}{\partial X^2} + \frac{\partial^2 C_f}{\partial Y^2}\right). \tag{5}$$

2.2 | Porous medium

Continuity:

$$\frac{\partial U_p}{\partial X} + \frac{\partial V_p}{\partial Y} = 0. \tag{6}$$

X-direction momentum equation:

$$\frac{\partial U_p}{\partial \tau} + \left(U_p \frac{\partial U_p}{\partial X} + V_p \frac{\partial U_p}{\partial Y}\right) = -\varepsilon^2 \frac{\partial P}{\partial X} + \frac{\varepsilon}{Re}\left(\frac{\partial^2 U_p}{\partial X^2} + \frac{\partial^2 U_p}{\partial Y^2}\right) - \varepsilon^2 \frac{I}{ReDa} U_p. \tag{7}$$

Y-direction momentum equation:

$$\frac{\partial V_p}{\partial \tau} + \left(U_p \frac{\partial V_p}{\partial X} + V_p \frac{\partial V_p}{\partial Y}\right) = -\varepsilon^2 \frac{\partial P}{\partial Y} + \frac{\varepsilon}{Re}\left(\frac{\partial^2 V_p}{\partial X^2} + \frac{\partial^2 V_p}{\partial Y^2}\right) - \varepsilon^2 \frac{1}{ReDa} V_p + \varepsilon^2 Ri\theta + \varepsilon^2 NRiC. \tag{8}$$

Energy equation:

$$\frac{\partial \theta_p}{\partial \tau} + U_p \frac{\partial \theta_p}{\partial X} + V_p \frac{\partial \theta_p}{\partial Y} = \frac{k_{eff}}{K_f PrRe}\left(\frac{\partial^2 \theta_p}{\partial X^2} + \frac{\partial^2 \theta_p}{\partial Y^2}\right). \tag{9}$$

2.3 | Mass equation of the species

$$\frac{\partial C_p}{\partial \tau} + U_p \frac{\partial C_p}{\partial X} + V_p \frac{\partial C_p}{\partial Y} = \frac{DR}{PrReLe}\left(\frac{\partial^2 C_p}{\partial X^2} + \frac{\partial^2 C_p}{\partial Y^2}\right). \tag{10}$$

The dimensionless parameters used in the equations above are defined as follows:

Prandtl number $Pr = \frac{\nu_f}{\alpha_f}$, Richardson number $Ri = \frac{\beta_{T,f} \rho_f g \Delta T H^3}{Re^2 \nu_f^2}$, Darcy number $Da = \frac{K}{H^2}$, Reynolds number $Re = \frac{u_{in} H}{\nu_f}$, buoyancy ratio $N = \frac{\beta_c \Delta C}{\beta_{T,f} \Delta T}$, Lewis number $Le = \frac{\alpha_f}{D_f}$, and mass diffusivity ratio $DR = \frac{D_{eff}}{D_f}$ where $DR = 0.533$.[22] The dimensionless temperature and

concentration are; $\theta = \frac{T - T_C}{T_H - T_C}$ and $= \frac{c - c}{c_H - c}$, respectively. The nondimensional velocities are characterized as $U, V = \frac{u, v}{U_{in}}$

The dimensionless boundary conditions are:

1- On the inlet of the channel

$$U = 1, V = 0, \theta = 0, C = 0.$$

2- On the outlet of the channel

$$\frac{\partial U}{\partial X} = 0, V = 0, \frac{\partial \theta}{\partial X} = 0, \frac{\partial C}{\partial X} = 0, P = 0.$$

3- On the solid adiabatic walls

$$U = 0, V = 0, \frac{\partial \theta}{\partial Y} = 0, \frac{\partial C}{\partial Y} = 0.$$

4- On the vertical left wall of the cavity:
Case 1: $U = 0, V = 0, \theta = 1, C = 1.$
Case 2: $U = 0, V = 0, \frac{\partial \theta}{\partial X} = 0, \frac{\partial C}{\partial X} = 0.$

5- On the vertical right wall of the cavity:
Case 1: $U = 0, V = 0, \frac{\partial \theta}{\partial X} = 0, \frac{\partial C}{\partial X} = 0.$
Case 2: $U = 0, V = 0, \theta = 1, C = 1.$

6- The boundary conditions along the inclined interface between the two media are:

$$\theta_f = \theta_p, \frac{\partial \theta_f}{\partial n} = \frac{k_{eff}}{k_f} \frac{\partial \theta_p}{\partial n}, \tag{11}$$

$$C_f = C_p, \frac{\partial C_f}{\partial n} = \frac{D_{eff}}{D_f} \frac{\partial C_p}{\partial n}. \tag{12}$$

The local Nusselt number is defined as;

$$Nu = \frac{hH}{k} = \frac{-\frac{\partial T}{\partial x} H}{(T_H - T_L)} = -\frac{k_{eff}}{k_f} \frac{\partial \theta}{\partial X}.$$

The average Nusselt number along the hot wall is;

$$Nu_{av} = \frac{1}{H} \int_0^H Nu dy. \tag{13}$$

The local Sherwood number is defined as;

$$Sh = -\frac{\partial C}{\partial X}.$$

Average Sherwood number is;

$$Sh_{\text{av}} = \frac{1}{H}\int_0^H Shdy. \tag{14}$$

3 | NUMERICAL METHODOLOGY

This problem is solved numerically using the Galerkin finite element method. The overall geometry is discretized with unstructured triangular elements and characterized as an assembly of finite elements in which the governing Equations (1) and (2) are discretized. Nodal approximated functions are assumed in the nodes of finite elements. To meet the inclined interface, triangular elements are used. Values of unknowns within the finite elements are recovered using nodal values.[23,24] To ensure and reach the convergence faster, the problem is solved transiently.

Each of the velocity distribution, temperature, and pressure are interpolated by selecting a basis function $\left[\Phi_i^k\right]_i^M$ for implementing approximation solutions for the velocity, temperature, and pressure distributions.

$$U, V \approx \sum_i^M (U, V)_i^k \Phi_i^k(X, Y), \theta \approx \sum_i^M \theta_i^k \Phi_i^k(X, Y), P \approx \sum_i^M \mathrm{P}_i^k \Phi_i^k(X, Y), \tag{15}$$

where the subscript i refers to the node number, superscripts k and M refer to time iteration and the number of nodes, respectively.

Then, the nonlinear residual equations that are obtained from the Galerkin weighted residual finite-element method are solved iteratively for each node using the Newton–Raphson iteration scheme. The iteration of the numerical solution is terminated when the percentage error between two successive computations reaches 10^{-3}, according to the

$$\left|\frac{\Gamma^{j+1} - \Gamma^j}{\Gamma^{j+1}}\right| \leq \eta, \tag{16}$$

j refers to the iteration number and Γ may be velocity, pressure, or temperature. Based on the unstructured triangular meshes, the domain is firstly subdivided using an automatic mesh-generating algorithm, which introduces finer elements close to the solid and irregular boundaries. The mesh independence solution is tested by refining the global mesh by increasing the elements based on the growth rate of 1.1 as depicted in Figure 2. For this test, the parameters are selected as $Le = 20$, $N = 0.5$, $Re = 150$, $H_{\text{p}} = 0.5$, $Da = 10^{-3}$ and the Richardson number (Ri) is altered from 0.01 to 100. Results of the average Nusselt number on the heated vertical wall qualify the mesh size of (12,161) where the elements show a mesh-independent

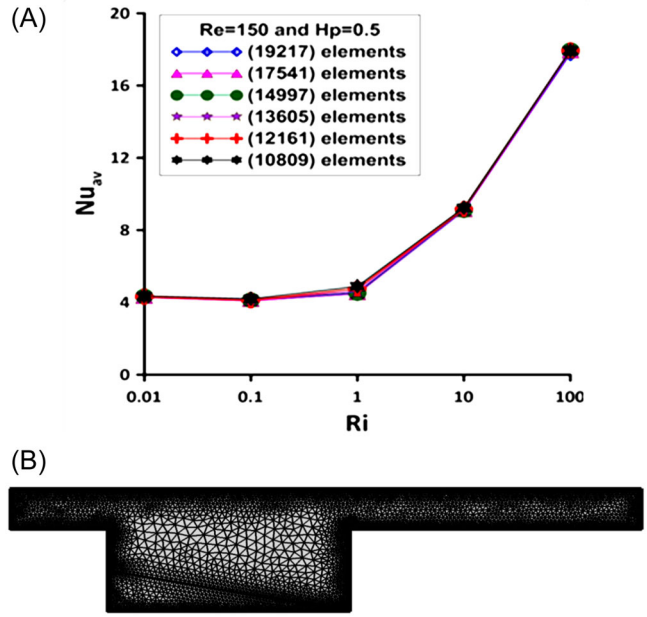

FIGURE 2 (A) Grid dependency tests with different Richardson number at $Re = 150$, $N = 0.5$, $Le = 20$, $H_p = 0.5$, $Da = 10^{-3}$. (B) The used mesh grid of 12,161 elements. [Color figure can be viewed at wileyonlinelibrary.com]

TABLE 1 Validation of the average Nusselt number with Manca et al.[2] for $Ri = 0.1$, $Re = 100$, and $Pr = 0.7$.

Heating mode	Present	Manca et al.[2]	% |Error|
Opposing forced flow	1.772	1.78	0.4494
Assisting forced flow	1.498	1.5	0.1333
Heating from below	1.631	1.65	1.1515

result. Figure 2B portrays the distribution of 12,161 elements used throughout the computations.

To validate the outcomes of the current numerical methodology, a case of laminar flow of air through a channel-open square cavity published by Manca et al.[2] is resolved. The other parameters of the compared case are illustrated in the caption of Table 1, which depicts a very good accuracy of average Nusselt numbers computed in two different numerical methods. Further validation with previous experimental work has been achieved as well. The experimental work of Leong et al.[25] concerned forced convection through three different geometries of graphite foam inserted in a channel and heated by constant heat flux. We validated our numerical code with one configuration namely, a block of graphite foam. The properties of the graphite foam are; pore diameter, $d_p = 0.31$ mm, thermal conductivity, $k_p = 72$ W/m K, and permeability, $K = 2.41 \times 10^{-10}$ m^2. The validation with the average Nusselt number is presented in Figure 3. Although there was some inconsistency, where the maximum error is 18% and the average error is 13.4%, we attribute this to the approximation we made in our code. Amongst these main approximations are the assumptions of the local thermal

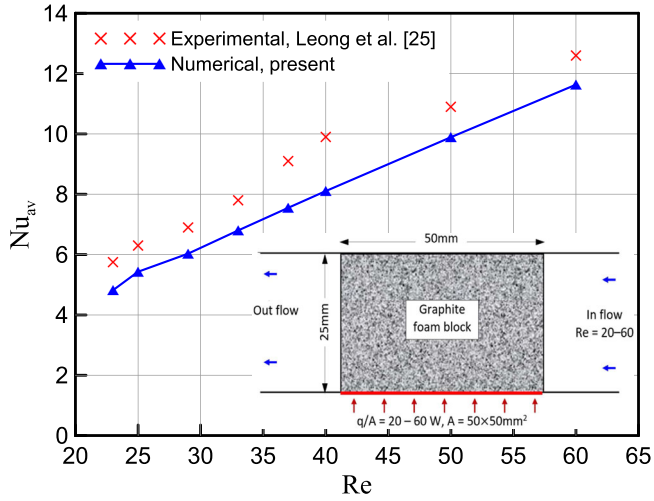

FIGURE 3 Validation with the experimental work of Leong et al.[25] [Color figure can be viewed at wileyonlinelibrary.com]

equilibrium and the constant properties of the graphite foam. In general, the present numerical methodology can safely be adopted.

4 | RESULTS AND DISCUSSION

To evaluate the role of the triangular porous layer and find plausible explanations, results are displayed by the average numbers of Nusselt Nu_{av} and Sherwood Sh_{av}, isotherms, isoconcentration lines, and streamlines. Reynolds, Richardson numbers, and the size of the triangular porous layer have been varied in two cases; assisting (heating from the left side of the cavity) and opposing (heating from the right side of the cavity). We fixed the following parameters at $Pr = 6.24$, $Da = 10^{-3}$, $Le = 20$, and $N = 0.5$. Computations have led to electing the best step of time equal to 0.01, which gives faster and most stable numerical solutions. All the following results are gathered at a steady state dimensionless time of $t = 80$, which is attained after several numerical runs.

4.1 | Assisting case

The left vertical wall of the cavity, in this case, is set at a higher temperature and concentration (active wall). Depending on the Hp value, it is worth mentioning that this wall is partially covered by the porous layer.

4.1.1 | Impact of Reynolds number

For various values of Reynolds number Re, the contours of streamlines, isotherms, and isoconcentration are portrayed in Figure 4 by setting $H_p = 0.5$ and $Ri = 1$. At $Re = 50$,

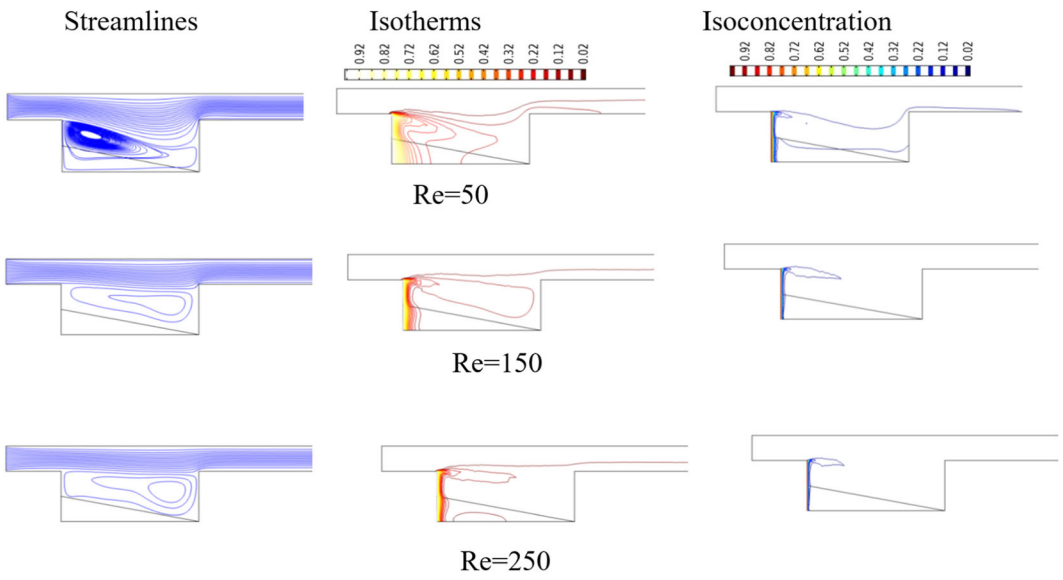

FIGURE 4 Streamlines, isotherms and isoconcentration contours for different Re at $Ri = 1$ and $H_p = 0.5$ for assisting forced flow. [Color figure can be viewed at wileyonlinelibrary.com]

a circulation is induced with its core close to the cavity's left wall and fluid penetrates into the porous domain because of the gravity force effect. At $Re = 150$ the cell is expanded with no penetrated fluid into the porous domain. Raising *Re* to 250, the circulation occupies most of the cavity due to the growth of the inertia force. Isotherms at $Re = 50$ are congregated close to the active left wall while heat diffuses toward the right wall of the cavity. This behavior is well expected because of the weak inertial force which leads to a thicker thermal boundary layer. On the other hand, increasing *Re* leads to clustered isotherms along the active wall because of the vigorous inertial force. Isoconcentration lines show that at low *Re* the species diffuses towards the right wall while increasing *Re* leads to conveying the species upward due to the start of vigorous buoyancy force.

Figure 5 portrays the variation of Nu_{av} with *Re* for various Ri at $H_p = 0.5$. No significant change in the Nu_{av} is seen when $Ri = 0.0$–0.1; however, the inception of Nu_{av} is recorded when the Richardson number is raised to $Ri \geq 1$. This behavior is well prospective because for a given Reynolds number, increasing Ri means boosting the free convection. The average Sherwood number exhibits the same trend as Nu_{av}.

4.1.2 | Impact of Richardson number

For various values of Richardson number *Ri*, the contours of streamlines, isotherms, and isoconcentration are portrayed in Figure 6 by fixing $H_p = 0.5$ and $Re = 150$. As $Ri = 0.1$, a circulation is induced along the cavity, and no penetration of the fluid to the porous layer because of the weak buoyancy force. Raising *Ri* to 1, the circulation expands slightly. When *Ri* increases to 100, a double-eye circulation behavior is dominated by a strong fluid pushed away to the porous layer, especially on the left active wall. Isotherms at $Ri = 0.1$ show a wider thermal boundary layer on the active wall where it is decreased when $Ri \geq 1$ which increases

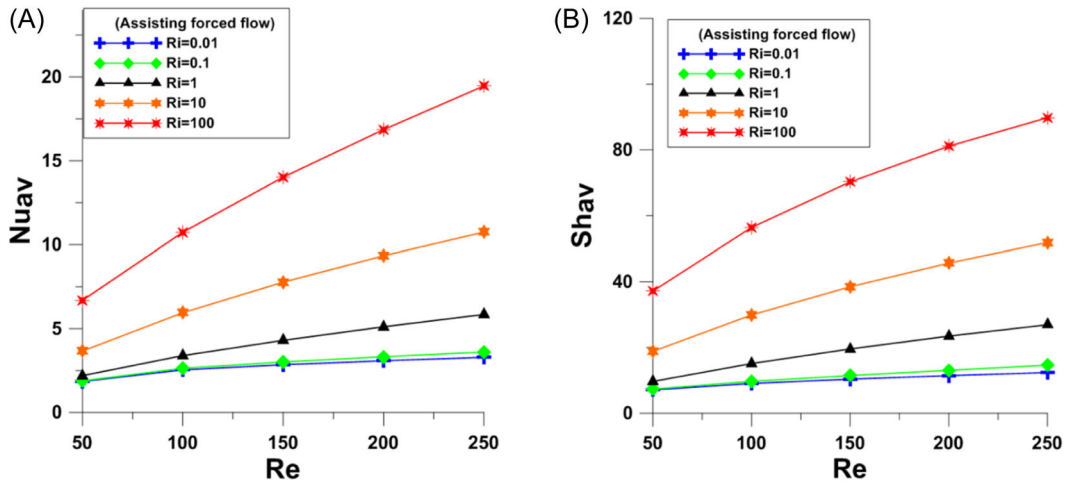

FIGURE 5 Variation of the average Nusselt (A) and Sherwood (B) numbers with Reynolds number for different values of Richardson number at $H_p = 0.5$ for assisting forced flow. [Color figure can be viewed at wileyonlinelibrary.com]

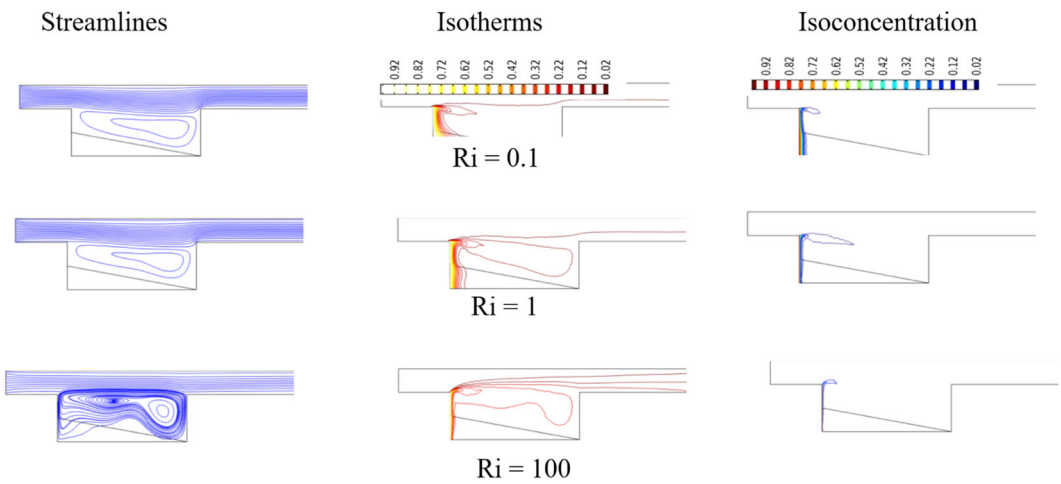

FIGURE 6 Streamlines, isotherms, and isoconcentration lines for different values of Ri at $Re = 150$ and $H_p = 0.5$ for assisting forced flow. [Color figure can be viewed at wileyonlinelibrary.com]

the heat removal from the left wall by the convective current. Concerning the isoconcentration lines of $Ri = 0.1$, species cluster close to the left wall where the boundary layer there rises while it decreases for $Ri \geq 1$ which leads to moving the species by the convective current towards the right wall.

Figure 7 depicts the development of Nu_{av} and Sh_{av} with Ri at $H_p = 0.5$. The figure emerges with less significant changes with Nu_{av} and Sh_{av} within $Ri = 0.01$–0.1 while they augment robustly beyond $Ri = 1$ because of the rising effect of the buoyancy force. In general, raising the Ri number strengthens the streamliners, stratifies the isotherms, and disturbs the isoconcentration lines.

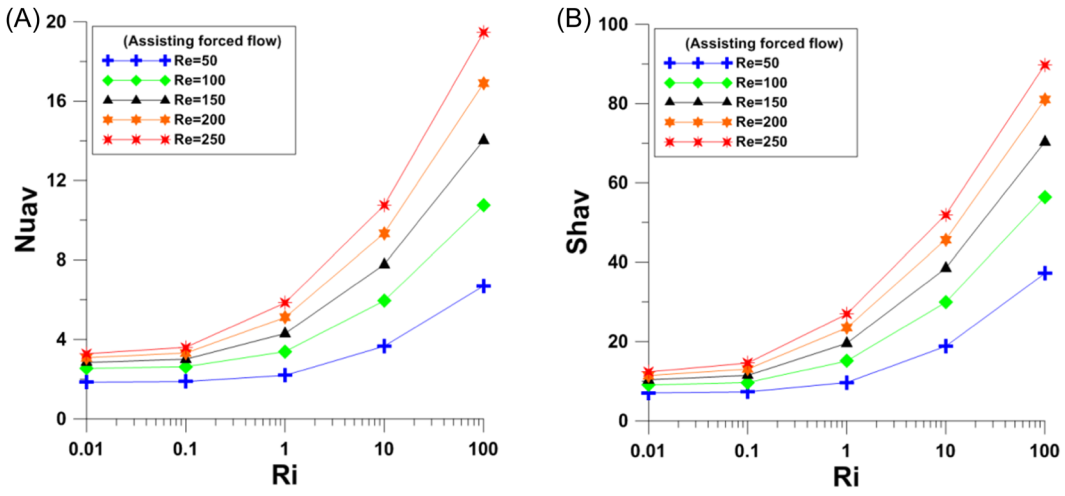

FIGURE 7 Variation of the average Nusselt number (A) and Sherwood number (B) with Richardson number for different values of Reynolds number at $H_p = 0.5$ for assisting forced flow. [Color figure can be viewed at wileyonlinelibrary.com]

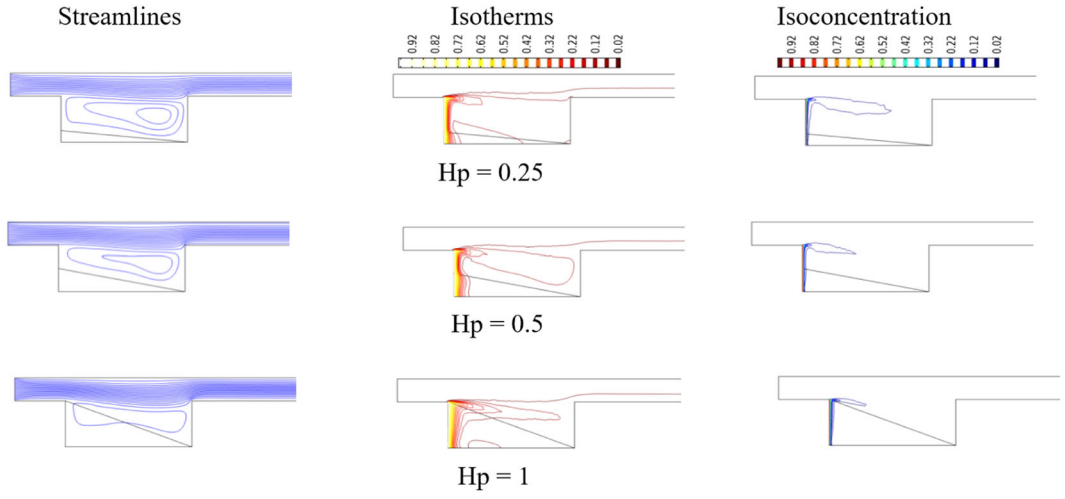

FIGURE 8 Streamlines, isotherms, and isoconcentration lines for different values of H_p at $Re = 150$ and $Ri = 1$ for assisting forced flow. [Color figure can be viewed at wileyonlinelibrary.com]

4.1.3 | Impact of the porous layer

The impact of the triangular porous layer size is characterized by its height Hp. Figure 8 shows that for a nearly horizontal layer (small H_p value), the circulation along the cavity experiences no penetration into the porous domain which is already a thin layer. When $H_p = 0.5$ the cell is squeezed along the fluid layer of the cavity. When H_p is set at $H_p = 1$ where the heat source is completely covered by a porous medium, the restriction becomes significant therefore, the recirculation retracts in the entire cavity. Isotherms with a thinner thermal boundary layer are

observed at $H_p = 0.25$, which means significant heat removal from the active left wall. While at higher H_p, the thermal boundary layer becomes thicker which results in weakened heat transfers. This can be referred to as the drag effect imparted by the porous domain that makes it experiences a thicker thermal boundary layer than that in the clear fluid. Isoconcentration lines show the diffusion of the species toward the right wall at a low porous layer thickness while the species congest along the active left wall when H_p increases.

Figure 9 displays the variations of Nu_{av} and Sh_{av} with H_p at $Ri = 1$ for different Re. Generally, both Nu_{av} and Sh_{av} decrease slightly with H_p. As such, another case of heating should be investigated to deeply inspect the role of the triangular porous domain.

4.2 | Opposing case

The right vertical wall of the cavity, in this case, is set at a higher temperature and concentration (active wall). It is worth mentioning that this wall faces the flow direction in the channel and it is completely subject to unrestricted fluid.

4.2.1 | Impact of Reynolds number

For various values of Reynolds number Re, the contours of streamlines, isotherms, and isoconcentration are portrayed in Figure 10 by setting $H_p = 0.5$ and $Ri = 1$. When $Re = 50$, a small circulation forms close to the left wall with no penetrating fluid into the porous domain while at $Re = 150$, the cell strengthens and fluid penetrates into the porous domain, and a secondary circulation is formed beside the large cell close to the right wall. When $Re = 250$, a double cellular behavior is seen where a small cell localizes near the lower right corner of the cavity. Isotherms at $Re = 50$ shows that the thermal boundary layer is limited close to the right

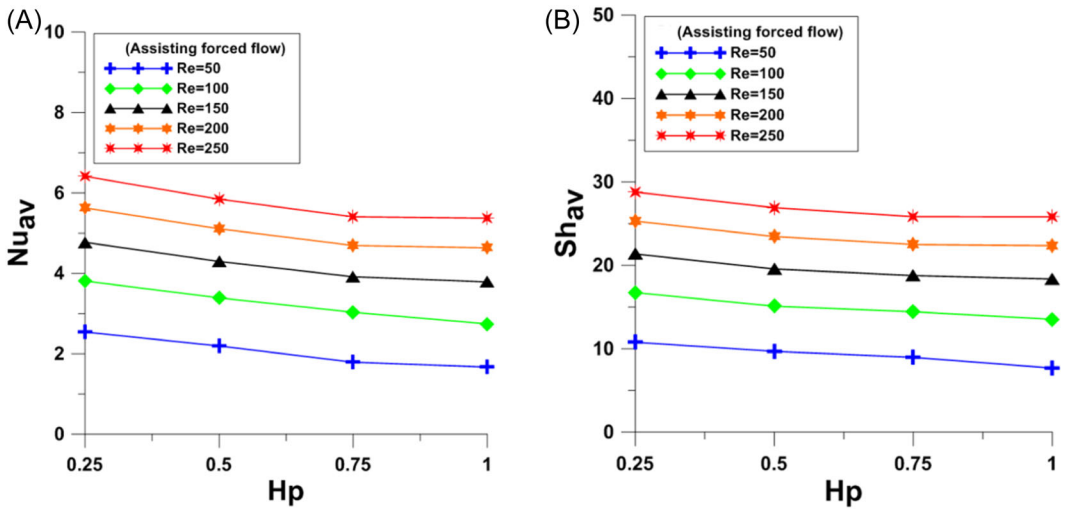

FIGURE 9 Variation of the average Nusselt number (A) and Sherwood number (B) with H_p for different values of Reynolds number at $Ri = 1$ for assisting forced flow. [Color figure can be viewed at wileyonlinelibrary.com]

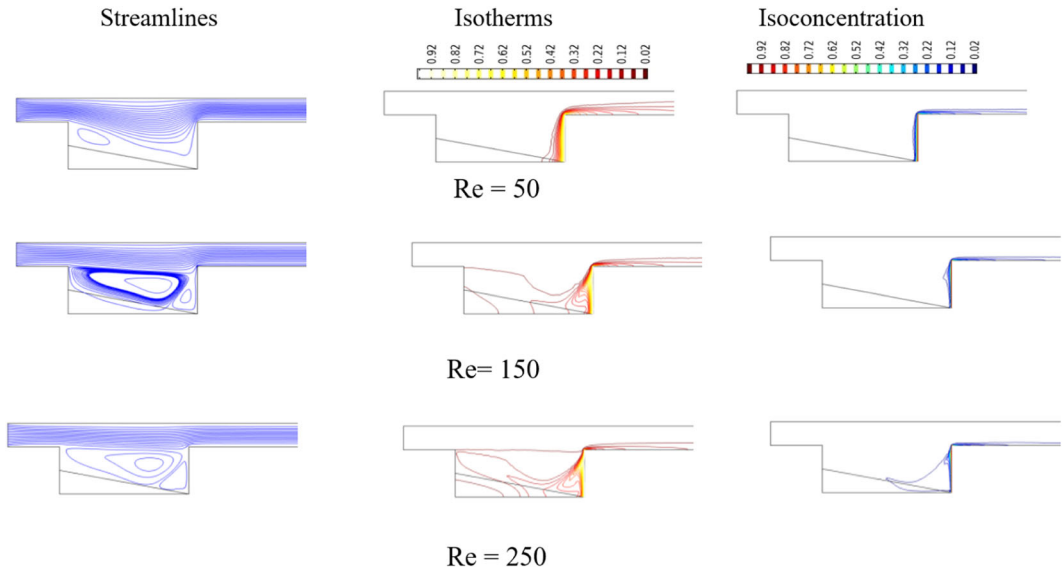

FIGURE 10 Streamlines, isotherms, and isoconcentration lines for different values of *Re* at $Ri = 1$ and $H_p = 0.5$ for opposing forced flow. [Color figure can be viewed at wileyonlinelibrary.com]

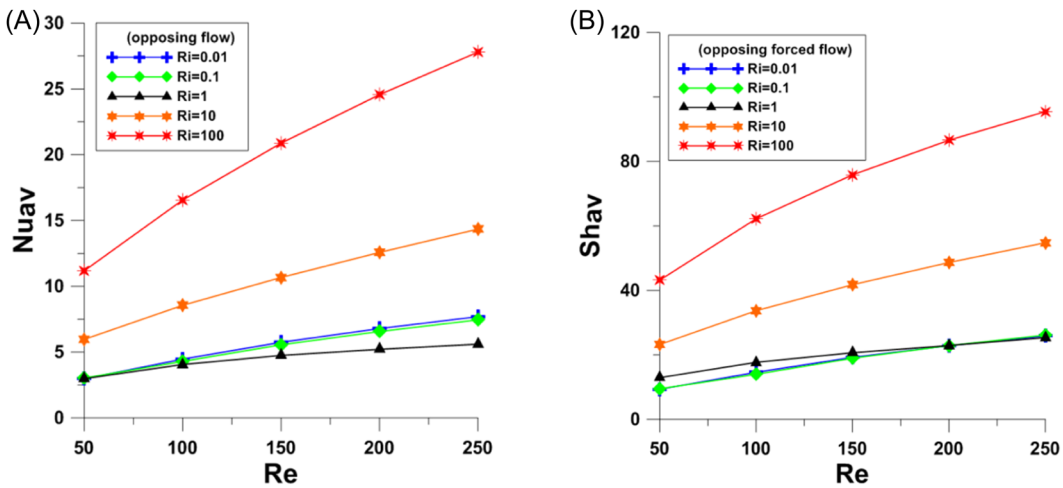

FIGURE 11 Variation of the average Nusselt (A) and Sherwood (B) numbers with Reynolds number for different values of Richardson number and $H_p = 0.5$, for opposing forced flow. [Color figure can be viewed at wileyonlinelibrary.com]

active wall and some temperature gradients are observed close to the exit channel part. When *Re* increases, the isotherms are randomly distributed within the cavity. This is because of the effective mixing resulting from the inertia force. The isoconcentration lines for $Re \leq 150$ are limited in a very thin solute boundary layer near the right cavity wall and lower wall of the exit channel. When $Re > 150$, the strong inertia force conveys the species from the right wall through the remainder of the cavity. The variation of Nu_{av} and Sh_{av} is plotted in Figure 11 with *Re* for different *Ri* at $H_p = 0.5$. There is no notable change in Nu_{av} when *Ri* increased from 0.01 to 1,

however, the minimum value of Nu_{av} is recorded at $Ri = 1$ because of the comparable natural and forced convection. At $Ri > 1$, the increase of Nu_{av} with Re is marginal because of the dominance of the buoyancy force. The Sh_{av} exhibits the same trend as Nu_{av}.

4.2.2 | Impact of Richardson

For various values of Richardson number Ri, the contours of streamlines, isotherms, and isoconcentration are portrayed in Figure 12 by fixing $H_p = 0.5$ and $Re = 150$. For $Ri \leq 0.1$, the strength of the induced circulation is insufficient to penetrate into the porous domain. For $Ri = 1$ (comparable convective modes) a double recirculation is observed where the secondary circulation localizes near the right corner of the cavity while fluid penetrates into the porous domain. Nevertheless, at $Ri > 1$, the cell is intensified along the cavity especially close to the hot wall, this implies the dominance of the natural convection. As a result, the fluid does not penetrate into the porous layer where a stagnant zone appears in the porous layer. Isotherms of $Ri \leq 1$ show that the strong recirculation serves in a robust exchange of heat thus, the isotherms spread out towards the left wall of the cavity. For $Ri > 1$, the gradient of temperature is restricted near the active hot wall. When Ri is raised to 100, the robust buoyancy force is distinguished by the temperature gradient close to the lower wall of the downstream channel. Concerning the isoconcentration lines of $Ri \leq 1$, species diffuse towards the left wall in the adjacency of the inclined interface due to the thermal diffusion and flow intensity. Otherwise, at $Ri > 1$, the species are clustered near the right active wall and the lower wall of the downstream channel.

Figure 13 explains the variation of Nu_{av} and Sh_{av} with Ri at $H_p = 0.5$. The figure shows a critical range of Richardson number that is when $Ri \leq 1$, Nu_{av} is invariable within the range $Re \leq 100$ while it declines slightly within the range $Re \geq 150$. For $Ri > 1$, a robust increase of Nu_{av} is observed within the whole studied range of Reynolds number. Hence, it can be deduced that the minimal Nu_{av} takes place when $Ri = 1$. The behavior is referred to the competition

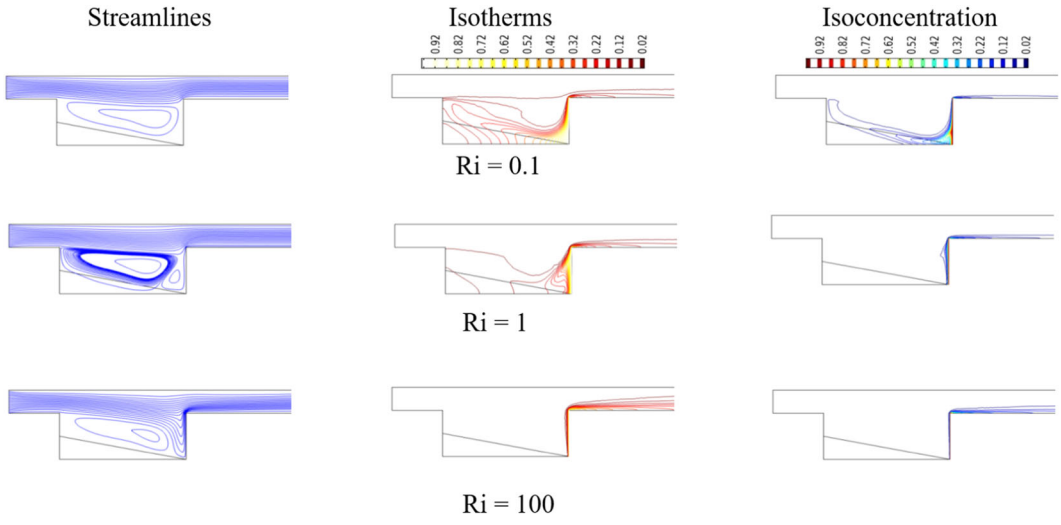

FIGURE 12 Streamlines, isotherms, and isoconcentration lines for different values of Ri at $Re = 150$ and $H_p = 0.5$ for opposing forced flow. [Color figure can be viewed at wileyonlinelibrary.com]

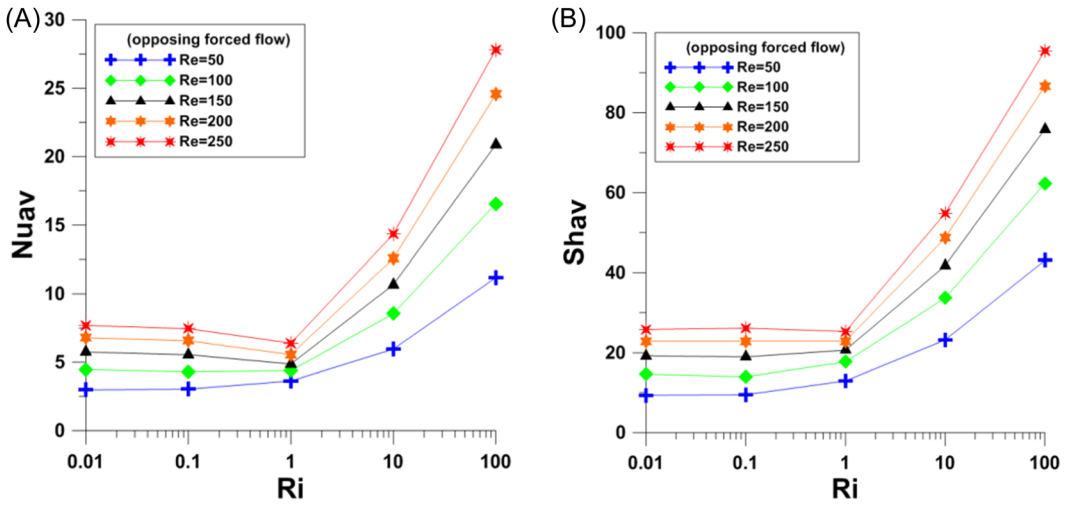

FIGURE 13 Variation of the average Nusselt (A) and Sherwood (B) numbers with Richardson number for different values of Reynolds number and $H_p = 0.5$ for opposing forced flow. [Color figure can be viewed at wileyonlinelibrary.com]

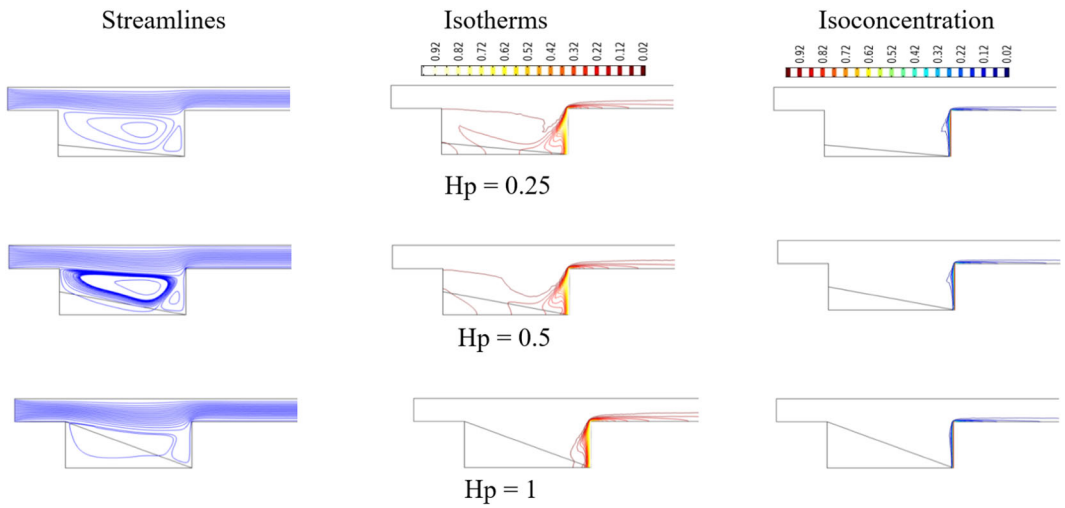

FIGURE 14 Streamlines, isotherms, and isoconcentration lines for different values of H_p at $Re = 150$ and $Ri = 1$ for opposing forced flow. [Color figure can be viewed at wileyonlinelibrary.com]

between the viscous and buoyancy forces. The Sh_{av} exhibits the same trend of the average Nusselt number.

4.2.3 | Impact of the porous layer

Figure 14 embodies the impact of the porous layer height H_p on the contours for $Re = 150$ and $Ri = 1$. At $H_p = 0.25$, a double cellular behavior is seen where a small cell is localized close to

the lower right corner of the cavity where the drag is minimal there. When $H_p = 0.5$, the main circulation strengthens and some fluid penetrates into the porous domain while the secondary circulation shrinks. As H_p is raised to its maximal value ($H_p = 1$), the circulation expands along the cavity with some penetrating into the porous layer. Isotherms portray that for $H_p \leq 0.5$, the robust double recirculation behavior serves in a significant exchange of heat where the isotherms spread out towards the left wall of the cavity, which is partly covered by the porous medium. While at $H_p > 0.5$, the recirculation of fluid within the cavity is weakened because of the raised drag imparted by the porous layer. As a result, the gradient of temperature is restricted near the hot active wall. Thereby, the rest of the cavity looks isothermal. Concerning the isoconcentration lines of $H_p \leq 0.5$, we see slight diffusion of species which results from the thermal convection. When $H_p > 0.5$, isoconcentration lines are clustered to the right wall and the lower wall of the downstream channel.

Figure 15 shows the variation of Nu_{av} and Sh_{av} as a function of H_p at different Re and $Ri = 1$. The role of H_p on Nu_{av} at $Re = 50$ can be ignored. Otherwise, at $Re > 50$, a slight change of Nu_{av} with H_p arises. Hence, the maximum value of Nu_{av} is recorded at $H_p = 1$. On the other hand, no significant changes in Sh_{av} are seen with increasing H_p.

4.3 | Comparison between assisting and opposing cases

This subsection addresses a comparison between the two cases, opposing and assisting to decide which case provides the efficient transport of heat and species within the prescribed domain. The behavior of Nu_{av} and Sh_{av} for the two cases with Re is presented in Figure 16 for (A) $Ri = 0.01$ and (B) $Ri = 100$. The figure indicates that the higher Nu_{av} and Sh_{av} are attained in the opposing case. The reasonable explanation of this finding relies on the direction of flow in the channel that is for the assisting case, the exchange between the active left wall and the fluid is restricted by the fluid circulation cell while in the opposing case, the fluid impinges the right active wall directly which robustly boost the exchange of heat and mass transfer. Therefore,

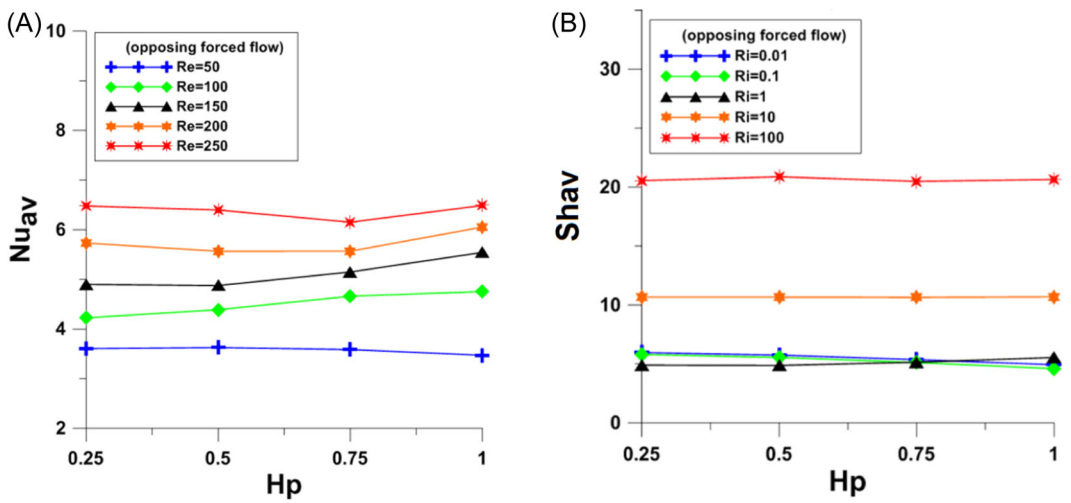

FIGURE 15 Variation of the average Nusselt (A) and Sherwood (B) numbers with H_p for different values of Reynolds number and $Ri = 1$ for opposing forced flow. [Color figure can be viewed at wileyonlinelibrary.com]

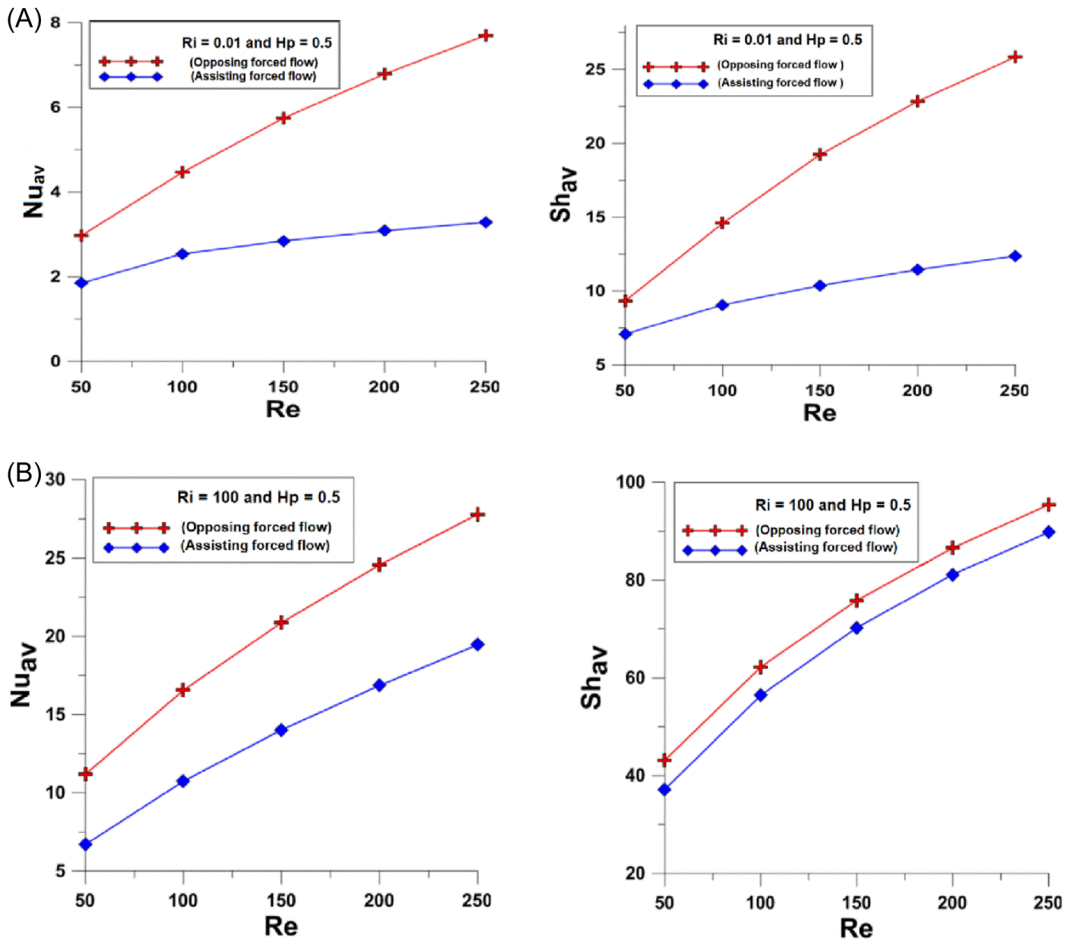

FIGURE 16 Comparison of the average Nusselt and Sherwood numbers between assisting and opposing forced flow with Reynolds number at (A) $Ri = 0.01$ and (B) $Ri = 100$. [Color figure can be viewed at wileyonlinelibrary.com]

Nu_{av} and Sh_{av} rise promptly with Re in the opposing case meanwhile mild increase is indicated in assisting case. This fashion is observed in both values of the Richardson number. At $Ri = 0.1$, the increase of Nu_{av} between the two cases are 61% and 134% for $Re = 50$ and 250, respectively. While for $Ri = 100$, the percentage increase of Nu_{av} are 67% and 43% at $Re = 50$ and 250, respectively.

4.4 | Correlations of the Nusselt and Sherwood numbers

To establish useful and shortened correlations for the average Nusselt and Sherwood numbers, data on these numbers were performed using regression analysis to get popular power low correlations. To make it easy and reliable with as high as possible correlation factor, the correlations are casted as in the following forms, $(Nu_{av}, Sh_{av}) = \begin{pmatrix} f(Re, Ri) & \text{for } H_p = 0.5 \\ f(Re, Hp) & \text{for } Ri = 1.0 \end{pmatrix}$:

4.4.1 | Correlations of assisting case

$$Nu_{av} = \begin{cases} 0.187Re^{0.645}Ri^{0.232} & (R^2 = 0.984) \\ 0.159Re^{0.632}H_p^{-0.162} & (R^2 = 0.993) \end{cases} \quad (17)$$

and

$$Sh_{av} = \begin{cases} 1.31Re^{0.556}Ri^{0.253} & (R^2 = 0.992) \\ 0.159Re^{0.653}H_p^{-0.107} & (R^2 = 0.996) \end{cases}. \quad (18)$$

4.4.2 | Correlations of opposing case

$$Nu_{av} = \begin{cases} 0.451Re^{0.553}Ri^{0.22} & (R^2 = 0.912) \\ 0.875Re^{0.359}H_p^{0.033} & (R^2 = 0.962) \end{cases}, \quad (19)$$

$$Sh_{av} = \begin{cases} 2.26Re^{0.497}Ri^{0.212} & (R^2 = 0.945) \\ 1.13 \times 10^{-7}Re^{3.396} + 3.89H_p^{-0.0475} & (R^2 = 0.958) \end{cases}. \quad (20)$$

Considerable attention was paid to establishing a correlation within the reliable criterion, $R^2 > 0.9$, therefore, Equation (20) which correlates the Sherwood number with Re and H_p appeared with combined power mode because of the limited role of Hp in the opposing case. However, Figure 17 displays the numerical results of the Nusselt number compared with those predicted by the established correlations for the assistance case.

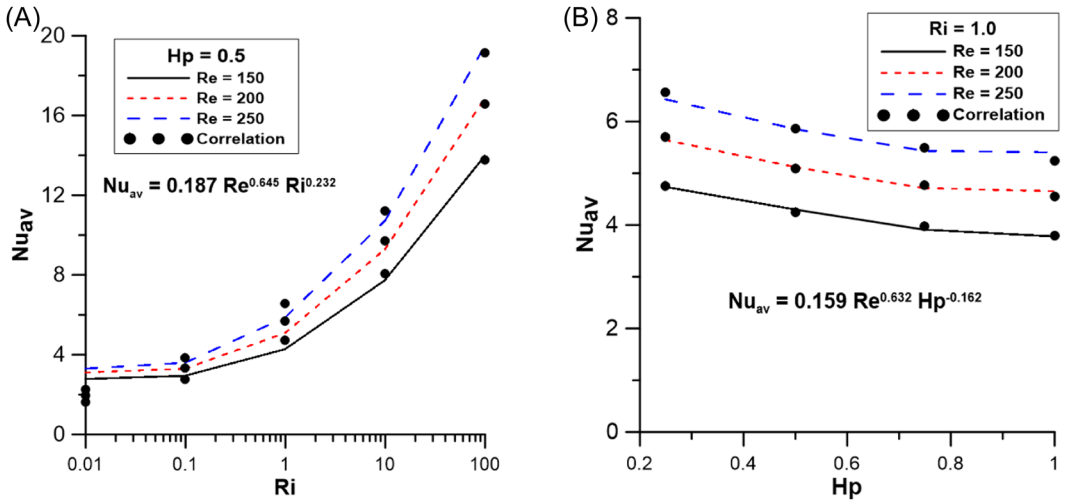

FIGURE 17 Predicted Nusselt number by the correlations for assistance case. [Color figure can be viewed at wileyonlinelibrary.com]

4.5 | Triangular and horizontal layers: A comparison study

To highlight the role of the triangular porous layer, we compared it with a rectangular layer (horizontal interface) for both cases, assisting and opposing. Figure 18 shows a comparison of Nu_{av} and Sh_{av} between the horizontal and triangular layers for the assisting case. The figure reveals no distinct role of the porous layer shape on the Nu_{av} at $Ri = 0.1$, however, at $Ri = 100$ the triangular porous layer experiences a slightly lower Nu_{av}. This implies that the porous layer geometry is inoperative in the assistance case. The Sherwood number depicts a different fashion, where for $Ri = 0.1$, the triangular layer shows lower Sh_{av}, while for $Ri = 100$, this layer shows higher than the horizontal one. Referring to the contour maps of the assistance case, it can be seen that the circulation is stronger in the upper part of the cavity and close to the right wall of the cavity. This strong circulation contributes to conveying more species.

The role of geometry of the porous layer for the opposing case is shown in Figure 19. Since the sources of heat and species are set on the right wall, therefore the triangular layer provides

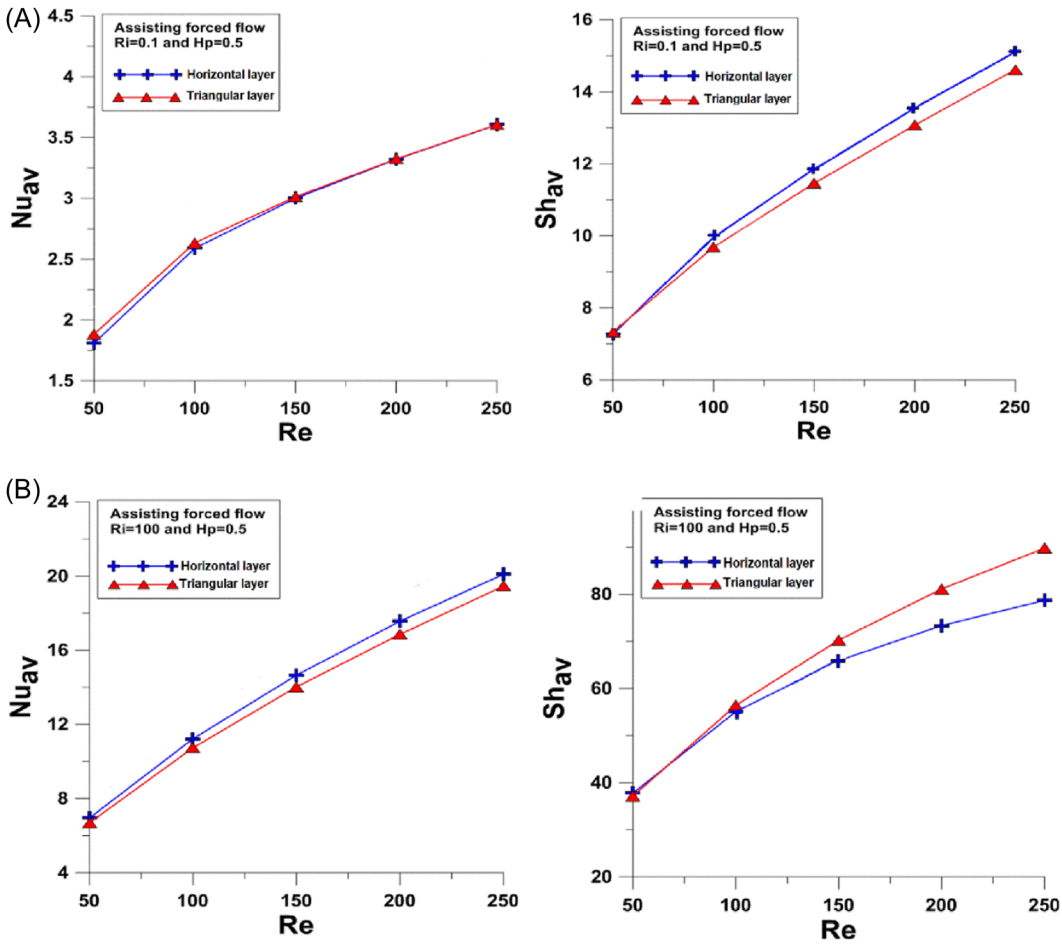

FIGURE 18 Comparison of the average Nusselt and Sherwood numbers between horizontal and triangular porous layers for assistance case at (A) $Ri = 0.1$ and (B) $Ri = 100$. [Color figure can be viewed at wileyonlinelibrary.com]

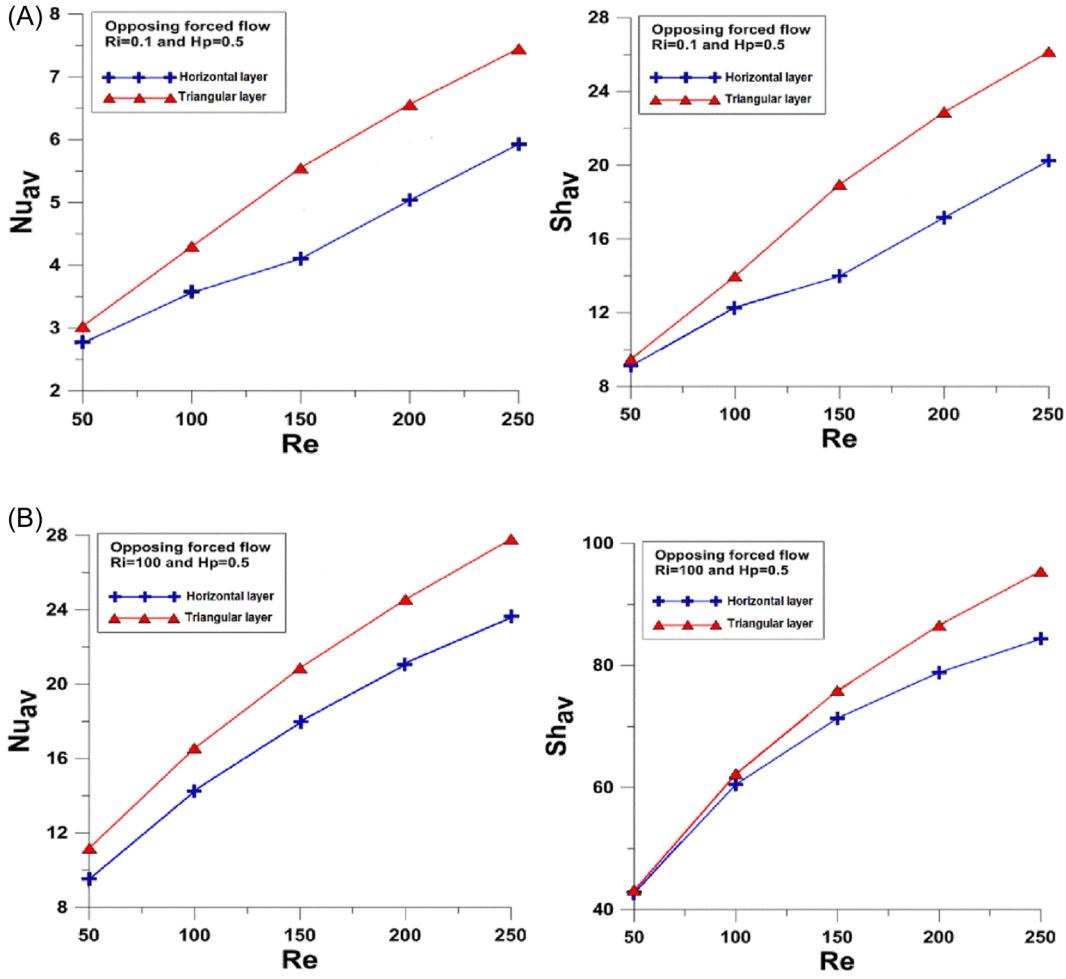

FIGURE 19 Comparison of the average Nusselt and Sherwood numbers between horizontal and triangular porous layers for opposing case at (A) $Ri = 0.1$ and (B) $Ri = 100$. [Color figure can be viewed at wileyonlinelibrary.com]

a free space for the forced fluid to hit the source and hence boosts the exchange of heat transfer and the transport of species. As such, the Nu_{av} and Sh_{av} values of the triangular porous layer are greater than the horizontal layer and for both $Ri = 0.1$ and 100. The percentage increase in Nu_{av} and Sh_{av} are 30% and 32% at $Ri = 0.1$, while the percentage increase at $Ri = 100$ are 16% and 9%, respectively. It can be inferred, therefore, that the transport of energy and species can be improved by setting the geometry of the porous layer in such a case that the forced flow directly blows the uncovered source of heat and species.

5 | CONCLUSIONS

The heat and species transfer in a composite cavity linked with a horizontal channel has been simulated numerically. The obtained results led to the conclusions listed below.

1- The triangular porous layer is a promising geometry that improves the heat and mass transfers by 30% and 32%, respectively more than the horizontal porous layer.
2- The opposing case gives maximum convective heat transfer, where for $Ri = 0.01$, the Nusselt number is higher by 61% and 134% for $Re = 50$ and 250, respectively, while for $Ri = 100$, the percentages increase are 67% and 43%.
3- Nusselt and Sherwood's numbers of the assisting case decrease with the size of the porous layer.
4- In the opposing case, the size of the triangular porous layer plays a notable role in the Nusselt number, while it does have a marginal role in Sherwood numbers.

NOMENCLATURE

c	dimensional concentration, kg/m^3
C	nondimensional concentration
C_p	specific heat, J/kg K
D	diffusivity of mass (m)
Da	Darcy number (K/H^2)
DR	ratio of mass diffusivity ($D_{\text{eff}}/D_{\text{f}}$)
g	gravitational acceleration, m/s^2
H	height of the cavity, m
H_{c}	height of the channel, m
H_{p}	height of the triangular porous layer, m
h	coefficient of convective heat transfer, W/m^2 K
k	thermal conductivity, W/m K
K	permeability of porous layer, m^2
L	width the cavity, m
Le	Lewis number ($\alpha_{\text{f}}/D_{\text{f}}$)
L_{d}	downstream length of the channel, m
L_{u}	upstream length of the channel, m
N	Buoyancy ratio ($\beta_{\text{C}}\Delta C/\beta_{\text{T}}\Delta T$)
Nu	Nusselt number (hH/k) m
p	pressure, N/m^2
P	nondimensional pressure ($\frac{p}{p_{\text{f}}^* u_{\text{in}}^2}$)
Pr	Prandtl number ($\nu_{\text{f}}/\alpha_{\text{f}}$)
Re	Reynolds number ($Re = u_{\text{in}}H/\nu_{\text{f}}$)
Ri	Richardson number ($Ri = Gr/Re^2$)
Sh	Sherwood number
T	dimensional temperature, K
T_{C}	inlet temperature of fluid, K
T_{H}	hot wall temperature, K
t	time, s
τ	dimensionless time $\left(\tau = \frac{t^* u_{\text{in}}}{H_{\text{c}}}\right)$
u, v	dimensional velocity components in x and y axes m/s
u_{in}	inlet velocity, m/s
U, V	dimensionless velocities component

x, y dimensional coordinates, m
X, Y dimensionless coordinate, $X = x/H_c$, $Y = y/H_c$

GREEK SYMBOLS

α thermal diffusivity m^2/s
β thermal expansion coefficient, K^{-1}
β_T thermal expansion coefficient, K^{-1}
β_c compositional expansion coefficient, m^3/kg
ε porosity of porous medium
θ dimensionless temperature $\left(\theta = \frac{T - T_C}{T_H - T_C}\right)$
ρ density of fluid, kg/m^3
μ dynamic viscosity, $N\,s/m^2$
ν_f kinematics viscosity of fluid, m^2/s

SUBSCRIPTS

av average
c cold
eff effective
f fluid
H hot, high
p porous
S solid

ACKNOWLEDGMENTS

The second author would like to acknowledge Al-Ayen University at Thi-Qar, Iraq for supporting and encouraging going ahead with novel research.

CONFLICT OF INTEREST

The authors declare no conflict of interest.

ORCID

Muneer A. Ismael https://orcid.org/0000-0001-9541-4940

REFERENCES

1. Nield DA, Bejan A. *Convection in Porous Media*. Springer; 2006.
2. Manca O, Nardini S, Khanafer K, Vafai K. Effect of heated wall position on mixed convection in a channel with an open cavity. *Numer Heat Transfer A*. 200343(3):259-282.
3. Leong JC, Brown NM, Lai FC. Mixed convection from an open cavity in a horizontal channel. *Int Commun Heat Mass Transfer*. 2005;32(5):583-592.
4. Brown NM, Lai FC. Correlations for combined heat and mass transfer from an open cavity in a horizontal channel. *Int Commun Heat Mass Transfer*. 2005;32(8):1000-1008.
5. Manca O, Nardini S, Vafai K. Experimental investigation of opposing mixed convection in a channel with an open cavity below. *Exp Heat Transfer*. 2008;21(2):99-114.
6. Aminossadati SM, Ghasemi B. A numerical study of mixed convection in a horizontal channel with a discrete heat source in an open cavity. *Eur J Mech-B/Fluids*. 2009;28(4):590-598.

7. Buonomo B, Manca O, Mesolella P, Nardini S. Numerical study on mixed convection in porous media in a channel with an open cavity below. Paper presented at: ASME International Mechanical Engineering Congress and Exposition 2010:1633-1641.
8. Nasrin R, Alim MA, Chamkha AJ. Numerical simulation of non-Darcy forced convection through a channel with nonuniform heat flux in an open cavity using nanofluid. *Numer Heat Transfer A*. 2013;64(10):820-840.
9. Buonomo B, Manca O, Marinelli L, Nardini S. Mixed convection in horizontal channels heated below with external heat losses on upper plate and partially filled with aluminum foam. Proceedings of the 5th International Conference on Porous Media and its Applications in Science and Engineering. 2014.
10. Carozza A, Manca O, Nardini S. Numerical investigation on heat transfer enhancement due to assisting and opposing mixed convection in an open ended cavity. Paper presented at: 2nd International Conference on Emerging Trends in Engineering and Technology. 2014:30-31.
11. Sabbar WA, Ismael MA, Almudhaffar M. Fluid-structure interaction of mixed convection in a cavity-channel assembly of flexible wall. *Int J Mech Sci*. 2018;149:73-83.
12. Saeid NH. Analysis of mixed convection in a vertical porous layer using non-equilibrium model. *Int J Heat Mass Transfer*. 2004;47(26):5619-5627.
13. Shi W, Vafai K. Mixed convection in an obstructed open-ended cavity. *Numer Heat Transfer A*. 2010;57(10):709-729.
14. Maougal A, Bessaïh R. Heat transfer and entropy analysis for mixed convection in discretely heated porous square cavity. *Fluid Dyn Mater Process*. 2013;9(1):35-58.
15. Mojumder S, Saha S, Rahman MR, Rahman MM, Rabbi KM, Ibrahim TA. Numerical study on mixed convection heat transfer in a porous L-shaped cavity. *Eng Sci Technol Int J*. 2017;20(1):272-282.
16. Gibanov NS, Sheremet MA, Ismael MA, Chamkha AJ. Mixed convection in a ventilated cavity filled with a triangular porous layer. *Transp Porous Media*. 2017;120(1):1-21.
17. Abd Al-Hassan AQ, Ismael MA. Numerical study of double diffusive mixed convection in horizontal channel with composite open porous cavity. *Spec Top Rev Porous Media*. 2019;10(4):401-419.
18. Almuhtady A, Alhazmi M, Al-Kouz W, Raizah ZA, Ahmed SE. Entropy generation and MHD convection within an inclined trapezoidal heated by triangular fin and filled by a variable porous media. *Appl Sci*. 2021;11(4):1951.
19. Abderrahmane A, Qasem NA, Younis O, et al. MHD hybrid nanofluid mixed convection heat transfer and entropy generation in a 3-D triangular porous cavity with zigzag wall and rotating cylinder. *Mathematics*. 2022;10(5):769.
20. Chamkha AJ, Ismael MA. Natural convection in differentially heated partially porous layered cavities filled with a nanofluid. *Numer Heat Transfer A*. 2014;65(11):1089-1113.
21. Sheremet MA, Trifonova TA. Unsteady conjugate natural convection in a vertical cylinder containing a horizontal porous layer: Darcy model and Brinkman-extended Darcy model. *Transp Porous Media*. 2014;101(3):437-463.
22. Ismael MA, Ghalib HS. Double diffusive natural convection in a partially layered cavity with inner solid conductive body. *Sci Iran*. 2018;25(5):2643-2659.
23. Rao SS. *The Finite Element Method in Engineering*. 5th ed. Elsevier; 2011.
24. Bathe KJ, Zhang H. Finite element developments for general fluid flows with structural interactions. *Int J Numer Methods Eng*. 2004;60(1):213-232.
25. Leong KC, Li HY, Jin LW, Chai JC. Numerical and experimental study of forced convection in graphite foams of different configurations. *Appl Therm Eng*. 2010;30(5):520-532.

How to cite this article: Al-Hassan AQA, Ismael MA. Effect of triangular porous layer on the transfer of heat and species in a channel-open cavity. *Heat Transfer*. 2022;1-24. doi:10.1002/htj.22741